

Characterization of solar cell passivating contacts using time-of-flight elastic recoil detection analysis

Cite as: Appl. Phys. Lett. **123**, 261106 (2023); doi: [10.1063/5.0174131](https://doi.org/10.1063/5.0174131)

Submitted: 28 August 2023 · Accepted: 3 December 2023 ·

Published Online: 27 December 2023



View Online



Export Citation



CrossMark

Yifu Shi,¹ Matthew Wright,¹ Matthew K. Sharpe,² Callum D. McAleese,² Jana-Isabelle Polzin,³ Xinya Niu,¹ Zimo Zhao,¹ Stephen M. Morris,¹ and Ruy S. Bonilla^{1,a)}

AFFILIATIONS

¹University of Oxford, Oxford OX1 3PH, United Kingdom

²Surrey Ion Beam Centre, University of Surrey, Guildford, Surrey GU2 7XH, United Kingdom

³Fraunhofer Institute for Solar Energy ISE, Heidenhofstr. 2, 79110, Freiburg, Germany

^{a)} Author to whom correspondence should be addressed: sebastian.bonilla@materials.ox.ac.uk

ABSTRACT

The unambiguous detection of hydrogen in solar cell contact structures is critical to understanding passivation and degradation phenomena. Deuterium is often used to depict the distribution of hydrogen more clearly. However, experimental noise and artifacts can hinder the clear identification of species. This work provides a report of time-of-flight elastic recoil detection (ToF-ERD) analysis to identify H/D contents in a thin poly-Si/SiO_x passivating contact. The structure contained a 1.3 nm interfacial SiO_x and an n⁺ doped poly-Si layer with a partly deuterated SiN_x coating. The samples were annealed to release H/D, and ToF-ERD was used to detect H/D in monatomic, singly charged forms, without the detection artifacts associated with conventional secondary ion mass spectroscopy. Chlorine ions were used to recoil surface species, which were analyzed to clearly and unambiguously resolve H and D. Depth profiles for the recoiled Si, N, O, D, and H atoms were calculated from the energy and velocity information registered after scattering events, which enabled the analysis of the structure of the multilayer stack. Even though the surface roughness and experimental limitations cause visible broadening of the profiles, which can hinder clear detection at the interfacial oxide, the ability to resolve hydrogen-related species makes ToF-ERD a significant and promising tool for studying the role of hydrogen in the performance and degradation of solar cell passivating contacts.

© 2023 Author(s). All article content, except where otherwise noted, is licensed under a Creative Commons Attribution (CC BY) license (<http://creativecommons.org/licenses/by/4.0/>). <https://doi.org/10.1063/5.0174131>

Passivating contacts based on doped poly-Si on thin oxide stacks have led to silicon cells with efficiencies exceeding 26%.¹ This approach is currently poised to surpass passivated emitter and rear cell (PERC) as the dominant silicon cell design, due to demonstrated higher efficiency potential in production.² The surface passivation in this contact approach depends on the hydrogenation of poly-Si and the underlying SiO_x interlayer, which involves a high-temperature H release from a H-rich dielectric layer.^{3–5} However, an excessive accumulation of hydrogen near the SiO_x interlayer can also cause degradation of the passivation.^{6–8} Therefore, it is critical to analyze and understand the distribution of hydrogen throughout the passivating contact after firing, with a particular interest in the presence of H near the SiO_x interlayer.

Direct detection of elemental H in Si structures is usually achieved with secondary ion mass spectrometry (SIMS), a common thin-film analysis tool in which the sample surface is under continuous ion beam sputtering to generate the secondary ions. However, reported

SIMS results for poly-Si on a SiO_x stack^{7,9,10} are susceptible to a spread-out and blurring of the H profile at the interfacial oxide, caused by measurement artifacts. This is due to (i) a displacement of H inward via knock-on from the primary beam¹¹ and (ii) changes of secondary ion yield as the solid matrices change during multi-layer sputtering, especially when profiling across an interface.^{12,13} Additionally, the detection sensitivity of H using SIMS is poor.¹⁴ Low-mass H-containing species are present ubiquitously in all vacuum systems. This residual H content arrives at and sticks to the sample surface during SIMS sputtering and is not differentiable from the intrinsic sample H content.^{15,16} As such, the residual gas contamination introduces large uncertainty in H quantification and increases the detection limit. To overcome such complication from environmental H, some prior works have used the isotope deuterium (²H/D).^{10,17} The detection limit of D is 10¹⁶ atom/cm³ and hence much lower than for H at over 10¹⁸ atom/cm³.^{12,14} The complex/molecular ion ¹H₂⁺ still overlaps with the ²D⁺ signal at 2 Da on the mass spectrum, leading to ambiguity over the

actual concentration of D in the sample. Because of the aforementioned limitations with SIMS, additional characterization approaches are required to provide a clearer understanding of the distribution of hydrogen through poly-Si on SiO_x passivating contacts, as well as a clear distinction between D and H profiles.

Time-of-flight elastic recoil detection (ToF-ERD) is an ion beam analysis technique that uses the elastic recoil process for signal ion generation.¹⁸ An incident primary beam with energy on the order of MeV (compared to keV for SIMS) is used at a near-glancing angle to knock or “recoil” atoms from within the sample. **Only elements lighter than the incident species can be detected with equal sensibilities;** hence, it is well suited for light elements including H.^{19,20} The recoiled atoms are then measured in two ways. First, their time-of-flight (ToF) between two timing foils is measured to describe the velocity of the recoiled atoms. Next, the atoms enter a gas ionization chamber (GIC) through a silicon nitride window, where the energy is measured. In this way, a histogram of detection events is recorded with the atoms’ ToF and measured energy, which shows elements grouping along different energy-vs-ToF curves. This enables greater mass separation of elements by ToF-ERD when compared to conventional ERD, which uses a solid-state energy detector with no information on velocities. The depth profiles for elements are calculated from the relationship of energy and velocity of recoiled atoms to the depth they escape from, with the highest energy and lowest ToF, for each element, relating to the surface.²¹ In contrast to SIMS, which continuously sputters away the matrix with a high fluence ion source, ToF-ERD is relatively non-damaging to the sample with a low total fluence below 1×10^{12} ions/cm². This means ToF-ERD is free of common SIMS sputtering artifacts including the ion beam mixing, complex ion formation, and continuous arrival of environmental H. As such, ToF-ERD can provide complementary information to SIMS in H detection. Reported hydrogen studies have used ERD with a He^+ (Ref. 22) or N^+ (Ref. 23) ion source to measure only the H or D content. A ToF-ERD setup can further enable measurements of more elements with greater mass separation from the ToF information.

In this Letter, we use ToF-ERD to analyze the distribution of D and H in partly deuterated poly-Si on SiO_x contact stacks. We show that ToF-ERD can be used to clearly differentiate and fully separate between D and H, which is a significant advantage in analyzing the role of hydrogenation in passivating contacts. The sample investigated in this work is shown in Fig. 1(a). The sample has a poly-Si on thin oxide structure with a dielectric SiN_x /H/D layer on top as the H/D source. The Si substrate is a shiny etched n-type float zone wafer. The

~ 1.3 nm SiO_x interlayer was thermally grown on the $200\ \mu\text{m}$ substrate. The 50 nm n^+ doped poly-Si layer was formed by plasma-enhanced chemical vapor depositing (PECVD) amorphous silicon (a-Si) and subsequently crystallizing at 900°C for 10 min in N_2 atmosphere. The 70 nm PECVD SiN_x /H/D deposition uses SiH_4 and ND_3 as gas precursors, resulting in partial D substitution. The sample was subsequently annealed on a hotplate at 500°C for 2 min for adequate H/D release. We further measured the surface roughness of the finished sample with a CoreAFM atomic force microscope (AFM) manufactured by Nanosurf.

Figure 1(b) shows a schematic of the ToF-ERD setup at the Surrey Ion Beam Center, which includes two timing foils for ToF and a gas ionization chamber (GIC) for the energy measurements. The detectors for recoiled atoms are placed at a scattering angle, θ , of 41° to the incident beam, where the incident and exit angles can be adjusted. In this work, both were set to 69.5° to ensure the best sensitivity along with mass and depth resolutions across the whole sample depth.^{24,25} A negative sputter ion source (HVE 860) creates negatively charged incident ions, which, using an injector magnet, are directed toward a 2 MV tandem accelerator. This accelerates the ions to the selected energy and switches the ions to positively charged. For these measurements, incident ion beams of 16 MeV $^{127}\text{I}^{8+}$ and 8 MeV $^{35}\text{Cl}^{6+}$ were used with energy dispersion below 10 keV. These energies were selected considering cross sections, count rate, and mass separation.²⁵ The energy of the Cl ions was lowered to 8 MeV to prevent the near-surface recoiled D from having enough energy to hit the back wall of the GIC and register the incorrect energy. For each incident ion species, the ToF-ERD measurement was run for 30 min with a beam spot of $3 \times 4\ \text{mm}^2$ controlled with slits before the sample chamber. The counts for coincidences occurring in both the second timing foil and the GIC were around 715 counts/s for Cl and 555 counts/s for I, with a background count of fewer than 20 counts/s. The ToF-ERD histograms were analyzed using the software Potku to eliminate any false coincidences due to incorrect ToF values, with elemental depth profiles outputted.²⁶

Figure 2 illustrates the histograms of detected true coincidences measured from ToF-ERD, displaying the energy measured by the detector and the ToF between the timing foils. In ERD data analysis, such a histogram is also referred to as a coincidence histogram. The results from using the chlorine $^{35}\text{Cl}^{6+}$ incident ionic species are displayed in Fig. 2(a) and iodine $^{127}\text{I}^{8+}$ in Fig. 2(b). Due to the different atomic masses, the detection events for different elements follow separated parabolic energy-vs-ToF curves as dictated by the relationship between kinetic energy, mass, and velocity. This allows for a clear distinction between the elements labeled next to each curve. Atoms recoiled from deeper in the sample will lose energy due to electronic stopping acting on incident ions on their way in and recoiled atoms on their way out, meaning that further along the parabola corresponds to deeper in the sample. A logarithmic color scale is used to show the density of detection counts, which can be related to the population of the element. Traces for the main elements of concern: Si, O, N, and C are shown clearly in both figures. Importantly, a trace for each H and D is observed at low energies. As the measurement relies on the different masses, an unambiguous distinction between H and D is observed. This clear differentiation between H and D highlights the strength of ToF-ERD to characterize deuterated passivating contacts, which could facilitate a stronger understanding of surface passivation and degradation.

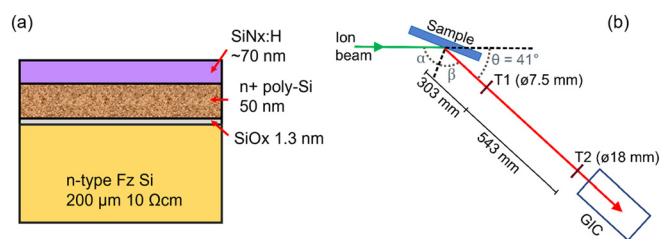


FIG. 1. (a) Schematic of the sample structure including a tunneling oxide and poly-silicon contact. (b) Schematic of the ToF-ERD experimental arrangement including direction of ion beam, timing foils (T1 and T2), and sample and detector positioning. α and β are incident and exit angle, respectively.

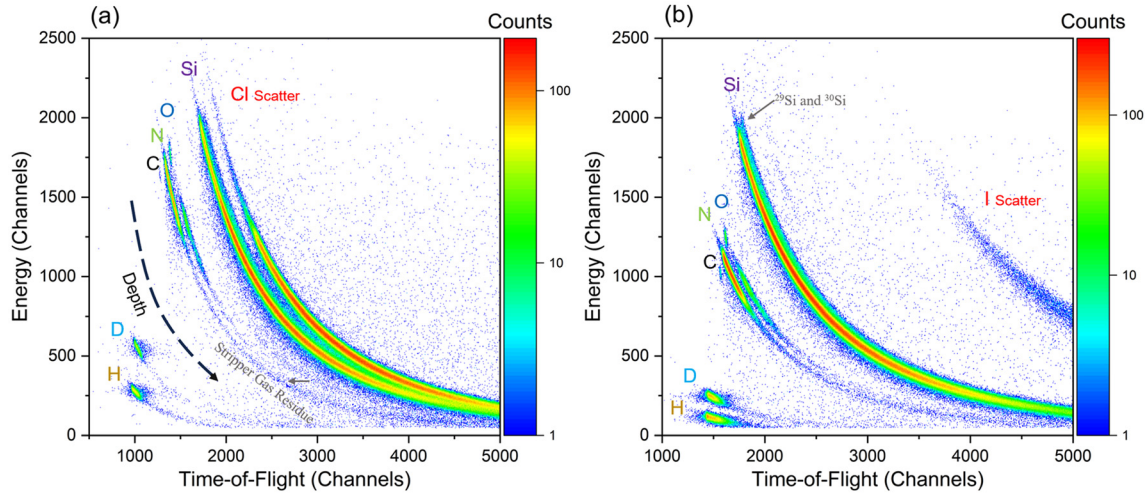


FIG. 2. ToF-ERD coincidence histograms from an incident beam of (a) 8 MeV $^{35}\text{Cl}^{6+}$ and (b) 12 MeV $^{127}\text{I}^{8+}$.

Compared to I, the Cl source enables H measurement deeper into the sample with better depth resolution due to the closer mass difference from Cl to H. The reason is that an ion with a similar mass to the lighter target atom will impart more energy compared to ion with a greater mass.²⁷ On the other hand, when using the I source we can avoid the overlap of the scattered Cl and Si at large depths and potentially see any other elements heavier than Cl. A trace of low energy N, as marked with the dark pointer in Fig. 2(a), is spotted on the Cl histogram. This is a minor experimental artifact that corresponds to the leakage N content from the stripper gas used in the accelerator to aid positive Cl ion production. The energy of such a leakage content is low and can only be translated to depths beyond concern, hence posing no effect on our measurements. The I histogram is leakage-free because minimal stripper gas is required for positive I ion production.

It is noteworthy that the poly-Si layer in the investigated sample contains phosphorous dopants. ToF-ERD using Cl source, however, does not deliver high enough mass separation between ^{30}Si and P to clearly see P. Hence, no P can be calculated from the coincidence histogram. It is known that the ToF-ERD mass resolution (for masses below the source atom) decreases with decreasing mass difference between source and target, due to increased dispersion of each curve in Fig. 2. The curve dispersion for each element is worsened by the presence of multiple isotopes, which can greatly increase the curve width for a particular element, such as the Si isotope group from 28 to 30. The mass separation can be improved by using a heavier and higher energy incident source, while a clear separation of ^{31}P from the Si group can be still challenging.

The coincidence histograms displayed in Fig. 2 can be converted into depth profiles for further analysis. To quantify the sample compositions from the experimental data of recoiled atoms, one must know the recoiling particle energy and the scattering cross section, the latter of which details the frequency of collisions occurring. For the atom recoiled from the surface, the energy following a collision with reference to the incident ion is given by²⁸

$$E_r = \left(\frac{4M_i M_r \cos^2 \theta}{(M_i + M_r)^2} \right) E_0,$$

where M_i and M_r are the mass of the incident and recoiling atom, respectively. E_0 is the energy transfer between the incident particle and target nucleus. θ is the angle of the recoiled atom, as shown in Fig. 1(b).

The differential scattering cross section for the recoiled atom at angle θ is given by²⁸

$$\frac{d\sigma_r}{d\Omega} \cong \frac{[Z_i Z_r e^2 (M_i + M_r)]^2}{(8\pi\epsilon_0 E_0 M_r)^2 \cos^3 \theta},$$

where σ_r is the scattering cross section of the recoiled atom, and Ω is the detector solid angle. Z_i and Z_r are the atomic number of the incident and recoiled atom, respectively. e is the elemental charge, and ϵ_0 is the vacuum permittivity.

To understand the distribution of atoms throughout the contact, we generated a depth profile. The elemental depth profile is dependent on the stopping force, which describes the energy loss of ions traversing the material. In the Potku software, the stopping force values are interpolated from tabulated values in a file library. The resulting ToF-ERD elemental depth profiles are outputted using a thin film unit (TFU) for depth scale, based on areal density for each element present in each depth layer. TFU scale is converted to nanometer scale following layer density assumptions such as²⁹

$$\frac{t[\text{TFU}]}{t[\text{nm}]} = \frac{\rho n N_A}{10^{22} m_r},$$

where t is the thickness, ρ is the density, n is the atoms per molecule, N_A is Avogadro's constant, and m_r is the molecular mass.

Figure 3 illustrates the ToF-ERD depth profiles for elements constructed from the representative Cl histogram, using Potku for the true coincidences. The converted nanometer depth scale is displayed as the top scale of the graph. The profiles are divided into regions suggested for each layer of the stack. A surface contamination layer containing

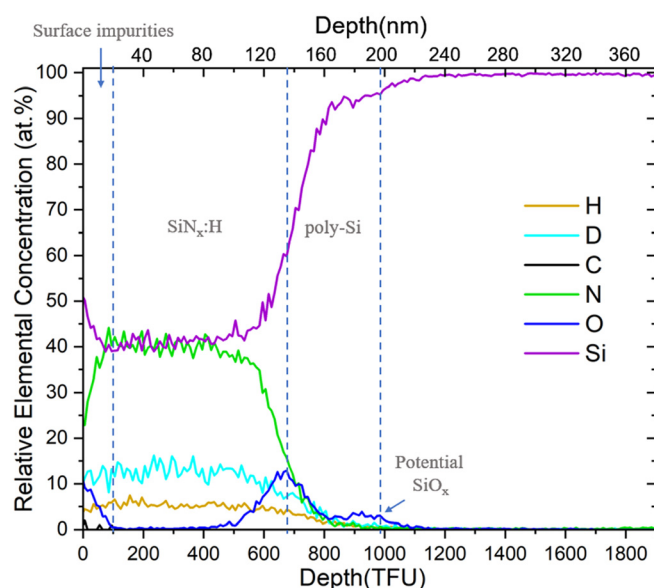


FIG. 3. Elemental depth profiles converted from ToF-ERD measurements from an incident beam of 8 MeV $^{35}\text{Cl}^{6+}$, for H, D, C, N, O, and Si. Note the depth given on both TFU scale and nanometer.

some C and O impurities is seen within the first 20 nm as expected from the handling contamination. Within the next 20–100 nm range is a clear SiN_x layer with roughly 1:1 Si and N. It is simplified here that all layers have the same density as c-Si at 2.33 g cm^{-3} , while the density of SiN_x film can range from $2.37\text{--}3.17 \text{ g cm}^{-3}$ depending on its stoichiometry and synthesis method. As a result, the nanometer thickness of SiN_x is subject to conversion error using these density assumptions, which can be improved by density measurements of the target materials. Average concentrations of D at 13.0 at. % and H at 5.4 at. % are detected in the 20–100 nm SiN_x range pointing to a D-rich dielectric source.

The gradual reduction of the N signal beginning after 100 nm, which falls from 38% to 1% over a 60 nm range, is indicative of the edge of the SiN_x layer. There are two broad O peaks observed as marked by the dashed lines at both boundaries of poly-Si: one centered close to 140 nm and the other smaller peak at ~ 200 nm. The first peak is thought to be related to the formation of an extra oxide on top of the poly-Si. The heavy doping in the poly-Si layer aids the formation of an unintentional native oxide. The nature of this peak is very broad, which is related to limitations caused by the roughness of the sample. We note that although the result shows a clear O peak on top of the poly-Si, this may not be fully representative of industrial TOPCon cells. Industrial processing requires strict control of the retention time between processes, meaning the unintentional oxide layer would be less pronounced. The second, smaller oxygen peak at ~ 200 nm is thought to be related to the actual interfacial oxide. Beyond this peak, the O content reaches 0% indicating the bulk c-Si. Beyond the SiN_x layer, the H and D contents both decreased; however, the ratio of the H to D increases. No evidence of an accumulation of H or D at the presumed $\text{SiO}_x/\text{c-Si}$ interface is observed, as opposed to results in Refs. 7 and 8.

The depth information beyond the SiN_x is limited for a variety of reasons. The first is related to the roughness of the sample. The samples used were chemically etched but not mechanically polished. Figure S1 in the supplementary material depicts the AFM surface topography map showing surface height variation over a $40 \times 40 \mu\text{m}^2$ area. The calculated root mean square roughness is 15.0 nm, which is much larger than the thickness of the interfacial tunneling oxide at ~ 1.3 nm. Such roughness causes depth concentration profiles to spread and effectively hinders the clear depiction of elements at the interfacial oxide. The second issue is related to the geometry of the experimental setup. With the incident and exit angles of 69.5° for the recoiled atoms, any roughness effect will be exaggerated due to the beam spreading across the surface. The final issue is an intrinsic limitation in ERD experiments related to scattering processes recoiled atoms experience when exiting the sample. For perfectly flat interfaces in a sample, the depth resolution of ToF-ERD can be around 1–3 nm but worsens when the interface is deeper into the material. When atoms come from deeper within, the scattering causes them to lose energy, resulting in larger uncertainty in the registered energy. This leads to a distortion of the depth profile, which becomes more pronounced at larger depths. To overcome these limitations, future experiments will include two key changes: (i) chemically mechanically polished samples should be used to reduce the impact of surface roughness and (ii) the front dielectric can be etched off to bring the interface closer to the surface, allowing for better depth resolution.

In conclusion, it is demonstrated that ToF-ERD is capable of unambiguously separating D and H contents in the poly-Si on a thin oxide passivation sample. Therefore, ToF-ERD is proposed as a strong supplementary technique for characterizing hydrogen distribution in passivating contact structures without H detection difficulties faced by SIMS. ToF-ERD experiments produce coincidence histograms showing separated species including Si, O, N, C, as well as H and D from the sample. A comparison of the results shows that an 8 MeV $^{35}\text{Cl}^{6+}$ incident beam source gives better profiling depth resolution at the cost of lower mass separation than the 12 MeV $^{127}\text{I}^{8+}$ source. The depth origin of detected signals is converted from the combined energy-ToF information and known material parameters to generate depth profiles. The two observed oxide peaks are attributed to the oxides both on top and at the bottom of the poly-Si. H/D contents can be quantified clearly in the top SiN_x layer. However, due to the surface roughness effect, depth profiles show layers intermixing and peaks broadening. The depth resolution can deteriorate further at higher depths. Samples with better surface flatness and shallower structures are proposed for future experiments.

See the supplementary material for details about the sample surface topography measured by atomic force microscope (AFM).

This work was supported by the UK Engineering and Physical Sciences Research Council Grant No. EP/V038605/1. Y.S. would like to thank the China Scholarship Council for funding his studies. M.W. acknowledges the funding provided by the UKRI Horizon Europe Guarantee MSCA Postdoctoral Fellowship scheme in the form of a Marie Skłodowska-Curie individual postdoctoral fellowship (Project No. 101109417). R.S.B. was supported by the Royal Academy of Engineering under the Research Fellowship

scheme (RF\201819\18\38). This work utilizes the ToF-ERD line in the Surrey Ion Beam Centre, which was originally developed at the University of Jyväskylä.

AUTHOR DECLARATIONS

Conflict of Interest

The authors have no conflicts to disclose.

Author Contributions

Yifu Shi: Data curation (supporting); Formal analysis (equal); Investigation (equal); Methodology (equal); Project administration (equal); Visualization (equal); Writing – original draft (equal); Writing – review & editing (equal). **Matthew Wright:** Conceptualization (equal); Formal analysis (equal); Investigation (equal); Methodology (equal); Project administration (equal); Supervision (equal); Validation (equal); Writing – review & editing (equal). **Matthew K. Sharpe:** Data curation (equal); Formal analysis (equal); Funding acquisition (equal); Investigation (equal); Methodology (equal); Resources (equal); Supervision (equal); Validation (equal); Visualization (equal). **Callum McAleese:** Data curation (equal); Formal analysis (equal); Investigation (equal); Visualization (equal). **Jana-Isabelle Polzin:** Conceptualization (equal); Data curation (equal); Investigation (equal); Methodology (equal); Writing – review & editing (equal). **Xinya Niu:** Data curation (supporting); Investigation (supporting). **Zimo Zhao:** Data curation (equal). **Stephen M. Morris:** Supervision (equal); Writing – review & editing (equal). **Ruy Sebastian Bonilla:** Conceptualization (equal); Formal analysis (equal); Funding acquisition (equal); Project administration (equal); Writing – review & editing (equal).

DATA AVAILABILITY

The data that support the findings of this study are available from the Oxford University Research Archive at ora.ox.ac.uk.

REFERENCES

- 1F. Haase, C. Hollemann, S. Schäfer, A. Merkle, M. Rienäcker, J. Krügener, R. Brendel, and R. Peibst, "Laser contact openings for local poly-Si-metal contacts enabling 26.1%-efficient POLO-IBC solar cells," *Sol. Energy Mater. Sol. Cells* **186**, 184–193 (2018).
- 2D. Chen, Y. Chen, Z. Wang, J. Gong, C. Liu, Y. Zou, Y. He, Y. Wang, L. Yuan, W. Lin, R. Xia, L. Yin, X. Zhang, G. Xu, Y. Yang, H. Shen, Z. Feng, P. P. Altermatt, and P. J. Verlinden, "24.58% total area efficiency of screen-printed, large area industrial silicon solar cells with the tunnel oxide passivated contacts (i-TOPCon) design," *Sol. Energy Mater. Sol. Cells* **206**, 110258 (2020).
- 3T. N. Truong, D. Yan, C. Samundsett, R. Basnet, M. Tebyetekerwa, L. Li, F. Kremer, A. Cuevas, D. Macdonald, and H. T. Nguyen, "Hydrogenation of phosphorus-doped polycrystalline silicon films for passivating contact solar cells," *ACS Appl. Mater. Interfaces* **11**(5), 5554–5560 (2019).
- 4B. Steinhäuser, F. Feldmann, D. Ourinson, H. Nagel, T. Fellmeth, and M. Hermle, "On the influence of the SiN_x composition on the firing stability of poly-Si/SiN_x stacks," *Phys. Status Solidi A* **217**(21), 2000333 (2020).
- 5B. W. H. van de Loo, B. Macco, M. Schnabel, M. K. Stodolny, A. A. Mewe, D. L. Young, W. Nemeth, P. Stradins, and W. M. M. Kessels, "On the hydrogenation of poly-Si passivating contacts by Al₂O₃ and SiN_x thin films," *Sol. Energy Mater. Sol. Cells* **215**, 110592 (2020).
- 6Y. Yang, P. P. Altermatt, Y. Cui, Y. Hu, D. Chen, L. Chen, G. Xu, X. Zhang, Y. Chen, P. Hamer, R. S. Bonilla, Z. Feng, and P. J. Verlinden, "Effect of carrier-induced hydrogenation on the passivation of the poly-Si/SiO₂/c-Si interface," *AIP Conf. Proc.* **1999**(1), 40026 (2018).
- 7D. Kang, H. C. Sio, J. Stuckelberger, R. Liu, D. Yan, X. Zhang, and D. Macdonald, "Optimum hydrogen injection in phosphorus-doped polysilicon passivating contacts," *ACS Appl. Mater. Interfaces* **13**(46), 55164–55171 (2021).
- 8C. Hollemann, N. Folchert, S. P. Harvey, P. Stradins, D. L. Young, C. Lima, S. De Souza, M. Rienäcker, F. Haase, R. Brendel, and R. Peibst, "Changes in hydrogen concentration and defect state density at the poly-Si/SiO₂/c-Si interface due to firing," *Sol. Energy Mater. Sol. Cells* **231**, 111297 (2021).
- 9T. N. Truong, D. Yan, W. Chen, M. Tebyetekerwa, M. Young, M. Al-Jassim, A. Cuevas, D. Macdonald, and H. T. Nguyen, "Hydrogenation mechanisms of poly-Si/SiO₂ passivating contacts by different capping layers," *Sol. RRL* **4**(3), 2070033 (2020).
- 10M. Lehmann, N. Valle, J. Horzel, A. Pshenova, P. Wyss, M. Döbeli, M. Despeisse, S. Eswara, T. Wirtz, Q. Jeangros, A. Hessler-Wyser, F. J. Haug, A. Ingenito, and C. Ballif, "Analysis of hydrogen distribution and migration in fired passivating contacts (FPC)," *Sol. Energy Mater. Sol. Cells* **200**, 110018 (2019).
- 11P. Van der Heide, *Secondary Ion Mass Spectrometry: An Introduction to Principles and Practices* (Wiley, 2014).
- 12Z. Zhu, V. Shuttanandan, and M. Engelhard, "An investigation of hydrogen depth profiling using ToF-SIMS," *Surf. Interface Anal.* **44**(2), 232–237 (2012).
- 13M. Cwil, P. Konarski, and J. Ciosek, "Ion mass interferences and matrix effects on SIMS depth profiling of thin Ti/Si multilayer films induced by hydrogen, carbon and oxygen contaminations," *Int. J. Mass Spectrom.* **263**(1), 54–58 (2007).
- 14F. A. Stevie, C. Zhou, M. Hopstaken, M. Saccomanno, Z. Zhang, and A. Turansky, "SIMS measurement of hydrogen and deuterium detection limits in silicon: Comparison of different SIMS instrumentation," *J. Vac. Sci. Technol. B* **34**(3), 03H103 (2016).
- 15K. Wittmaack, "Background formation in SIMS analysis of hydrogen, carbon, nitrogen and oxygen in silicon," *Nucl. Instrum. Methods Phys. Res.* **218**(1–3), 327–332 (1983).
- 16C. W. Magee and E. M. Botnick, "Hydrogen depth profiling using SIMS—Problems and their solutions," *J. Vac. Sci. Technol.* **19**, 47–52 (1981).
- 17G. Dingemans, W. Beyer, M. C. M. Van De Sanden, and W. M. M. Kessels, "Hydrogen induced passivation of Si interfaces by Al₂O₃ films and SiO₂/Al₂O₃ stacks," *Appl. Phys. Lett.* **97**(15), 152106 (2010).
- 18P. Trocellier and T. Sajavaara, "Elastic recoil detection analysis," in *Encyclopedia of Analytical Chemistry* (Wiley, 2008).
- 19Z. Siketić, I. B. Radović, I. Sudić, and M. Jakšić, "Surface analysis and depth profiling using time-of-flight elastic recoil detection analysis with argon sputtering," *Sci. Rep.* **8**(1), 10392 (2018).
- 20Z. Siketić, I. B. Radović, and M. Jakšić, "Quantitative analysis of hydrogen in thin films using time-of-flight elastic recoil detection analysis," *Thin Solid Films* **518**(10), 2617–2622 (2010).
- 21K. Yasuda, "Time-of-flight ERDA for depth profiling of light elements," *Quantum Beam Sci.* **4**(4), 40 (2020).
- 22R. Sharma, S. Vajandar, T. Osipowicz, J. B. Li, A. G. Aberle, and Y. Huang, "Hydrogen diffusion from PECVD silicon nitride into multicrystalline silicon wafers: Elastic recoil detection analysis (ERDA) measurements and impact on light and elevated temperature induced degradation (LeTID)," *AIP Conf. Proc.* **2147**(1), 140009 (2019).
- 23T. Matsui, M. Bivour, M. Hermle, and H. Sai, "Atomic-layer-deposited TiO₂ Nanolayers function as efficient hole-selective passivating contacts in silicon solar cells," *ACS Appl. Mater. Interfaces* **12**(44), 49777–49785 (2020).
- 24J. Julin and T. Sajavaara, "Conceptual study of a heavy-ion-ERDA spectrometer for energies below 6 MeV," *Nucl. Instrum. Methods Phys. Res. B* **406**, 61–65 (2017).
- 25S. Giangrandi, T. Sajavaara, B. Brijs, K. Arstila, A. Vantomme, and W. Vandervorst, "Low-energy heavy-ion TOF-ERDA setup for quantitative depth profiling of thin films," *Nucl. Instrum. Methods Phys. Res. B* **266**(24), 5144–5150 (2008).
- 26K. Arstila, J. Julin, M. I. Laitinen, J. Aalto, T. Konu, S. Kärkkäinen, S. Rahkonen, M. Raunio, J. Ikonen, J. P. Santanen, T. Tuovinen, and T. Sajavaara, "Potku—New analysis software for heavy ion elastic recoil detection analysis," *Nucl. Instrum. Methods Phys. Res. B* **331**, 34–41 (2014).
- 27W. Chu, *Backscatter Spectrometry* (Academic Press Inc., San Diego, 1978).
- 28W. Assmann, H. Huber, C. Steinhäuser, M. Dobler, H. Glückler, and A. Weidinger, "Elastic recoil detection analysis with heavy ions," *Nucl. Instrum. Methods Phys. Res. B* **89**(1–4), 131–139 (1994).
- 29L. Mikkö, *Improvement of Time-of-Flight Spectrometer for Elastic Recoil Detection Analysis* (University of Jyväskylä, 2013).